ELSEVIER

International Journal of Heat and Fluid Flow 21 (2000) 542–553

International Journal of HEAT AND FLUID FLOW

www.elsevier.com/locate/ijhff

Structural features and surface heat transfer associated with a row of short-hole jets in crossflow

Charles A. Hale, Michael W. Plesniak *, Satish Ramadhyani

Maurice J. Zucrow Laboratories, School of Mechanical Engineering, Purdue University, 1003 Chaffee Hall, West Lafayette, IN 47907-1288, USA

Abstract

Surface streak experiments coupled with flow visualization and numerical simulations were used to investigate short length-to-diameter injection holes for geometries of interest to the gas turbine industry. The flow field results were also related to measured surface heat transfer coefficients in the downstream region of the jets. Geometric surface topology maps inferred from "oil and lampblack" surface streak experiments give insights into the flow field, as well as boundary layer disruption, and ultimately the convective heat transfer coefficient enhancement in the wake region of the jets. A secondary counter-rotating vortex pair (CRVP) with the opposite sense of rotation as the well-documented main CRVP is present in some configurations and is found to noticeably enhance the attachment event in the wake region and correspondingly enhance the convective heat transfer coefficient. The separation and attachment regions corresponding to the separation and attachment of boundary layer fluid brought about by jet–crossflow interaction was found to strongly affect the heat transfer on the surface downstream of the jets. The relative strength of the attachment events, and therefore the effect on *h*, is dependent on the trajectory of the CRVP, presence or absence of the secondary CRVP, and the attachment of crossflow fluid that has accelerated around the issuing jet. In addition to providing information about the crossflow boundary layer disruption, the surface topological results relate the signature of the surface shear stress to the coherent flow structures in the flow field being investigated.

Keywords: Gas turbine; Film cooling; Jet-in-crossflow; Heat transfer; Short holes

1. Introduction

Demands for higher thermal efficiencies in modern gas turbines or have prompted designers to steadily increase first-stage gas inlet temperatures to a level that necessitates aggressive cooling schemes. Turbine inlet temperatures of 1900 K are typical of current designs, and there is interest in elevating the temperatures even higher. Such temperatures are well above the failure temperature of the blade material.

One method of protecting airfoils in these harsh environments is discrete-hole film cooling. Cooler, denser air is bled from the compressor and fed through internal passages in the blade or vane. The coolant then flows from the internal passages and impinges on the internal surface of the blade before turning to flow through a narrow internal plenum. From the supply plenum, the coolant is injected through small discrete holes into the external boundary layer, forming a protective film on the surface. Prediction of discrete-hole film-cooling performance requires an improved understanding of the fundamental jet-in-crossflow. The jet-in-crossflow has been studied extensively for over 50 years, as discussed in a review paper by Margason (1993). However, many issues remain unresolved, as reported most notably by Morton and Ibbetson (1996), Haven and Kurosaka (1997), Kelso et al. (1998), Fric and Roshko (1994), Findlay et al. (1999), Yuan and Street (1998), Smith and Mungal (1998), and Brizzi et al. (1997) as well as others.

Pietrzyk et al. (1989, 1990), Sinha et al. (1991b), Sen et al. (1994), Schmidt et al. (1994), Bons et al. (1994), and Kohli and Bogard (1995) investigated different aspects of film cooling performance for short injection holes ($L/D \leqslant 4$). The holes were supplied by a large, low-speed reservoir, or plenum, which fed normal to the film cooling hole. Various short hole numerical studies, e.g., by Walters and Leylek (1996, 1997), Berhe and Patankar (1996) and Ferguson et al. (1998), have used the above experimental measurements as benchmarks. Instantaneous PIV velocity data in the jet–crossflow region were reported by Gogineni et al. (1996) for $L/D = 2.4$. Berhe and Patankar (1996) also investigated a narrow plenum ($1 < H/D < 4$) configuration in the region of a plenum endwall, where all of the fluid flowing through the plenum exits through the film cooling holes.

The first studies to address a narrow flow channel were conducted by Wittig et al. (1996) who presented preliminary results for an experimental and numerical study of a single jet-in-crossflow fed by a narrow channel ($H/D = 2$). The work was extended by Thole et al. (1996, 1997), Gritsch et al. (1997),

---

* Corresponding author. Tel.: +1-765-494-1537; fax: +1-765-494-0530.

E-mail address: plesniak@ecn.purdue.edu (M.W. Plesniak).

PII: S0142-727X(00)00043-6

Notation

D	diameter of the film cooling hole
DR	density ratio $= (\rho_j/\rho_\infty)$
h	convective heat transfer coefficient, $q'' = h(T_\mathrm{w} - T_\infty)$
k	thermal conductivity
L	length of film cooling hole
M	blowing ratio $= (\rho_\mathrm{j} U_\mathrm{j}/\rho_\infty U_\infty)$
P	spanwise spacing (pitch) of film cooling holes
q''	heat flux
Re	Reynolds number
T_∞	freestream temperature
T_j	jet temperature
T_w	wall temperature
U_∞	time averaged freestream velocity
U_j	jet cross-sectional average velocity
u_τ	friction velocity, $\sqrt{\tau_\mathrm{w}/\rho}$
$X(M)$	Euler characteristic $= \sum$ nodes $- \sum$ saddles
X	streamwise distance downstream from center of hole
Y	distance normal to wall
$y+$	inner variable wall normal coordinate $(= yu_\tau/\nu)$
Z	spanwise distance from center of hole
Greeks	
α	streamwise injection angle
δ	boundary layer 99% thickness
δ^*	boundary layer displacement thickness
ρ_j	jet air density
ρ_∞	freestream air density
θ	boundary layer momentum thickness
τ_w	wall shear stress

and Kohli and Thole (1997, 1998). In this series of studies, the authors are careful to differentiate between channels feeding the film cooling holes (in which all of the flow through the channel does not flow through the film cooling hole) and the narrow plenum introduced by Berhe and Patankar (1996). The implications of these studies are well summarized by Kohli and Thole (1998).

Burd et al. (1996) reported hydrodynamic measurements comparing 35° streamwise injection for injection hole length-to-diameter ratios of 7.0 and 2.3. They found significant differences in the penetration of the jet into the crossflow and the region of influence downstream of the jet. This study was extended by Burd and Simon (1997) to investigate the plenum geometry effects. The same L/D ratios were investigated, but a plenum with a height of 2D delivered coolant flow co-current to the crossflow (co-flow) and counter-current to the crossflow (counter-flow) for some of the $L/D = 2.3$ cases. Significant differences in surface film cooling effectiveness values in the near hole region were found as the plenum flow direction was changed. These results contradicted the numerical results of Berhe and Patankar (1996), which indicated the effect of plenum flow direction to be negligible for $H/D = 2$. In a continuation of this effort, Burd and Simon (1998a,b) reported discharge coefficients and turbulence spectra and length scale data for the same cases.

The current investigation examined the effects of plenum and injection hole geometry on the flow physics and heat transfer associated discrete-hole film cooling. The configuration is highly idealized with respect to turbomachinery hardware and the study was not meant to examine film cooling performance of any specific configurations at engine conditions. The objective was to relate the hydrodynamics and structural features of the flow field associated with a row of jets-in-crossflow to the surface heat transfer performance. The results are relevant to current advanced design interest for first stage vanes in which the thin wall thickness results in length-to-diameter ratios $(L/D) < 3$. Under these conditions, the flow exiting the coolant hole is far from fully developed and there is strong coupling between the coolant supply and the external crossflow. Due to length restrictions, this paper will focus primarily on the effects of plenum flow direction on short $(L/D = 0.66)$ 90° holes only. Results for 35° angled holes are available in Hale et al. (1999a,b,c). Velocity profiles for both cases have been reported by Hale (1999) and Brundage et al. (1999). While angled film cooling holes are currently used in most turbine applications, normal (90°) holes are attractive from a manufacturing perspective for advanced thin-walled vane designs.

2. Experimental facility

The experiments were carried out in an open circuit low-speed wind tunnel with a 122 cm long by 30 cm square, optically-clear, polycarbonate test section. A detailed description of the low-speed tunnel is given by Wolochuk et al. (1994, 1996). The freestream turbulence intensity is less than 0.5% over the operating range, and the scale of the turbulence is small, as the flow is conditioned in an upstream settling chamber by a honeycomb and a series of increasingly fine screens, the last of which has is a #42 mesh with 41% solidity. The jet injection region attaches to the floor of the test section, and the boundary layer which encounters the row of jets is conditioned using a 1.3 mm diameter cylindrical trip wire spanning the width of the wind tunnel floor. The trip wire was designed according to the criteria given by White (1974). It is located 0.66 m upstream of the leading edge of the film cooling holes. A secondary blower supplies the injection air to the cooling holes through a narrow plenum.

“Adiabatic” floors were constructed from polystyrene, “Styrofoam” ($k = 0.026$ W/m K). The supply plenum is reversible such that co-flow or counter-flow plenum geometries are available. In all cases the plenum height is one hole diameter (1D) with the plenum end wall is 0.66 D past the edge of the hole. This configuration is different than a transverse serpentine cooling passage arrangement that is commonly used in many current designs. It is motivated by proposed advanced designs of stator vanes which will have dead-end passages with high-speed flow travelling parallel to or counter to the crossflow. The plenum attaches directly to the adiabatic floor of the tunnel as shown in Fig. 1. The experimental parameters of the study are given in Table 1. While the scaled geometric parameters are of interest to the gas turbine industry, the experimental conditions do not replicate density ratios, freestream turbulence levels or length scales, Mach numbers, or surface curvature associated with real engine conditions.

3. Experimental procedures

During the course of the study, various diagnostic methods were used to reveal the presence of coherent structures and assess their impact on the heat transfer coefficient. A canonical boundary condition (uniform heat flux) was imposed to evaluate the heat transfer coefficient. In an actual turbine blade, the thermal boundary condition will conform to neither the uniform heat flux nor the uniform wall temperature canonical conditions, and indeed, it is necessary to consider the complete

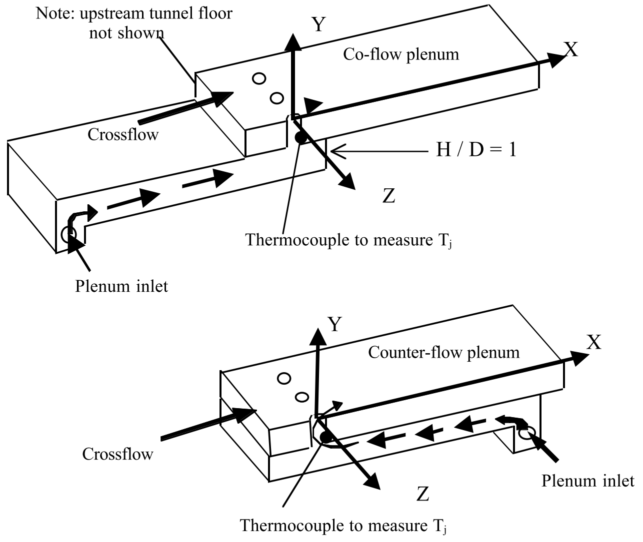

Fig. 1. Schematic of adiabatic test section and plenum (not to scale).

heat conduction problem in the blade. Heat transfer coefficients in turbulent flows are relatively insensitive to the thermal boundary condition, but caution should be exercised in extending these results to turbine environments, especially in regions of separation and flow reversal.

The oil-and-lampblack technique is a well-developed method used to visualize the mean surface shear stress distribution in boundary layers. In the current study, the surface streak experiments were performed by fitting white contact paper over the injection plate region, coating the surface with a tracer and recording the resulting pattern while the tunnel was operated. Since lampblack is not readily available, a substitute tracer was developed. It consisted of 1 part copy machine toner, 2 parts kerosene-based fog juice, and 7 parts baby oil. Once the mixture was applied, the wind tunnel and secondary blower were turned on simultaneously. The ensuing transient behavior was recorded with a Canon ES 1000 8 mm video camera and the steady state surface streak pattern was photographed using a Nikon FM2 camera.

In order to measure the convective surface heat transfer coefficient, h, where $q'' = h(T_w - T_\infty)$, a thin film heater was placed into the adiabatic floe constructed from extruded polystyrene ($k = 0.026$ W/m K). The heater was comprised of two copper bus bars spanning the streamwise length of the heater and a 0.0254 mm thick piece of stainless steel foil shim stock acting as the resistor. A schematic of the thin film heater is shown in Fig. 2. The stainless steel heater provided constant heat flux (q'') over its surface area when supplied with current from a power supply with 800 amp capability. The uniformity of the heat flux on the heaters was measured (using liquid crystal thermography, as described below) to evaluate their suitability once they were installed on the surface. The heaters were rejected unless the heat flux was uniform over the surface within 5% under ambient "free convection" conditions. The uniformity of the heat flux under forced convection was verified for canonical flat plate boundary layer conditions, with no film cooling jets. There was no spanwise variation in the convective heat transfer coefficient data for the flat plate condition, except outside the region where data were taken (the bus bar-thin foil contact point and copper bus bar region). The experimental values compared well with values predicted by an unheated starting length flat plate empirical correlation (Kays and Crawford, 1980), see Hale (1999) for details regarding heat flux surface testing and performance.

The heater surface was coated with cholesteric liquid crystal paint (Hallcrest 28c1W) on a flat black background. The mass flow rate of the injection air was monitored by the orifice plate flow meter with an embedded thermocouple to account for changes in air density with temperature. The crossflow freestream velocity was monitored using a pitot-static tube measuring the dynamic head with a micro-manometer with a resolution of 0.025 mm of water. The blowing ratios (M) were calculated based on the plug flow jet-exit velocity associated with the total jet injection mass flow rate.

The temperature of the injection air and the freestream air were the same (approximately room temperature). The jet temperature was maintained at the freestream temperature using a constant temperature bath flowing through a compact heat exchanger at the inlet of the secondary injection blower. A numerical model was utilized to evaluate the conduction losses through the Styrofoam ($k = 0.026$ W/m K) substrate. The losses through the Styrofoam into the injection hole and into the plenum were predicted to be negligible. A thermocouple in

Table 1
Parameters

Hole diameter (D)	19 mm
Number of holes	5
Hole spanwise spacing (P/D)	3.0
Free stream velocity (U_∞)	10 m/s
Freestream turbulence intensity (u'/U_∞)	<0.5%
Blowing ratio ($M = \rho_j u_j / \rho_\infty U_\infty$)	0.5, 1.0, 1.5
Hole length-to-diameter ratio (L/D)	0.66 (90° jets)
Plenum feed direction	Co-flow, counter-flow
Plenum height (H/D)	1
Endwall distance (E/D)	0.66
Boundary layer parameters (measured at jet hole leading edge location)	
BL displacement thickness (δ^*/D)	0.10–0.15
BL momentum thickness (θ/D)	0.09
BL Reynolds numbers	
(Re_θ)	1020
(Re_δ)	10,500
(Re_{δ^*})	1430
(Re_x)	1.4×10^6
Jet Reynolds number (Re_D)	12,000 ($M = 1.0$)

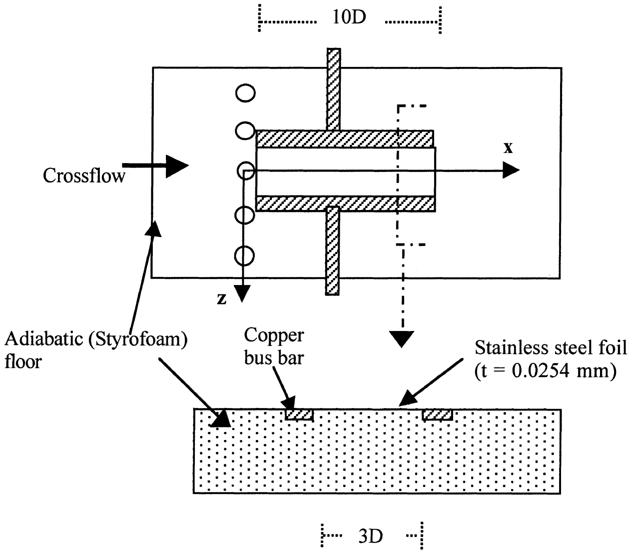

Fig. 2. Adiabatic floor containing heater (not to scale).

the injection hole was placed near the plenum, slightly protruding into the flow field to monitor the jet inlet temperature. In as much as the thermal conductivity of the test floor was extremely small and the predicted losses were negligible, this thermocouple measurement was an accurate representation of the gas temperature at the inlet and exit of the injection hole. A thermocouple was also placed in an adjacent hole directly in the flow field inside the jet, and the two thermocouples measures were the same.

The tunnel freestream temperature was also monitored with a thermocouple. The jet and freestream thermocouples were calibrated against each other using the same constant temperature bath at various temperatures and agreed with each other within the readability of the electronic thermocouple reading device (0.2°C). The same thermocouples were used for the in situ calibration of the liquid crystal paint. A narrow, 2.8 nm bandwidth optical filter was used in conjunction with a SONY model MVC-FD7 digital camera to record isotherms at 514 nm (only one temperature contour, i.e., liquid crystal color corresponding to 514 nm, was measured on the wall at a time). The narrow bandwith filter passed only 1% of the visible spectrum for a 1°C bandwidth liquid crystal paint, resulted in highly resolved surface temperature measurements. The isotherms were calibrated against the thermocouples in regions of low thermal gradients on the adiabatic floor. The calibration was repeated for each set of experiments and whenever changes in lighting or camera angle were made.

During the course of the experiments, different surface heat flux values resulted in different spatial locations of the isotherms observed through the narrow-band optical filter, and therefore different h values. The constant heat flux value was calculated using the measured dimensions of the heater, the resistivity of the heater material and the measured current. Over the operating range of the experiments, the viscosity of the fluid at the wall was estimated to vary by a maximum of 5% due to variations in the surface temperature.

A 3D finite-volume heat conduction analysis of the near-hole region was conducted to calculate the conjugate heat transfer losses to the boundary layer plate. The model of the experimental configuration used to measure the convective heat transfer coefficient utilized a computational domain consisting of the polystyrene floor, thin stainless foil film heater, and the copper bus bars. The domain extended from the downstream edge of the injection hole to thirteen diameters downstream of the injection hole and consisted of 100,000 cells. In order to correct the convective heat transfer coefficient data, the energy loss due to conduction effects was computed. This was accomplished by integrating the predicted heat transfer from the exposed surface of the stainless steel heater and subtracting the value from the total volumetric generation in the heater. The numerical model indicated that the most significant conduction losses through the Styrofoam substrate were localized at the edges, where the copper bus bars resulted in conjugate effects. The losses through the Styrofoam into the injection hole and into the plenum were predicted to be negligible and conjugate heat conduction effects within the thin film heater were also insignificant. The numerical solutions indicate that (highly localized) conduction losses into the substrate were up to 10% of the total heat generation in the thin film heater. These losses were accounted for in computing the surface heat flux values used to determine the convective heat transfer coefficient values, i.e., the numerically-predicted conjugate effects were used to correct the raw data.

4. Experimental uncertainty

The experimental uncertainties were calculated using standard uncertainty analysis methods (Kline and McClintock, 1953). The uncertainty in the temperature ranged from 1% to 7% of the wall-to-freestream temperature difference depending on the operating temperatures, and the uncertainty of the surface heat flux was 5.8%. The calculated uncertainties for the convective heat transfer coefficient values range from 6% to 9%. It is worth noting that the uncertainty associated with the change in resistivity of the stainless steel heater was 4%, and this value was included in the uncertainty of the convective heat transfer coefficient instead of modeling the temperature distribution in the heater. The spatial locations obtained in digitizing the isotherm data were found to be repeatable within 1%.

5. Numerical techniques

The computations of the fluid flow field and heat transfer were performed using FLUENT software on an IBM RS 6000 workstation with 512 Mb of random access memory. The commercial software package GeoMesh was used to generate the geometry and mesh. The domain includes the narrow plenum, the injection hole, and the crossflow region. The geometry was generated in the CAD package contained in GeoMesh and the structured body-fitted mesh was created using the object oriented, parametric block modeling tool P-Cube contained in the GeoMesh package. The grid was generated by specified node bunching using Eriksson interpolation schemes. The grid was also smoothed using Thomas–Middlecoff relaxation schemes. An example of the computational domains is shown in Fig. 3 and a magnified view of the near-hole grid at the jet exit plane is shown in Fig. 4. The upstream boundary layer velocity profile was approximated with a curve fit of the experimentally measured boundary layer profile, located four diameters upstream of the injection hole. The measured turbulence parameters for the conditioned boundary layer at the leading edge of the injection holes are given in Table 1 were input to the numerical stimulation.

The low Mach number Reynolds-averaged Navier–Stokes equations were solved using second-order upwind discretization schemes and various turbulence models and near-wall-treatment. This formulation allows the simulation of the effects of differences in density due to temperature differences in the

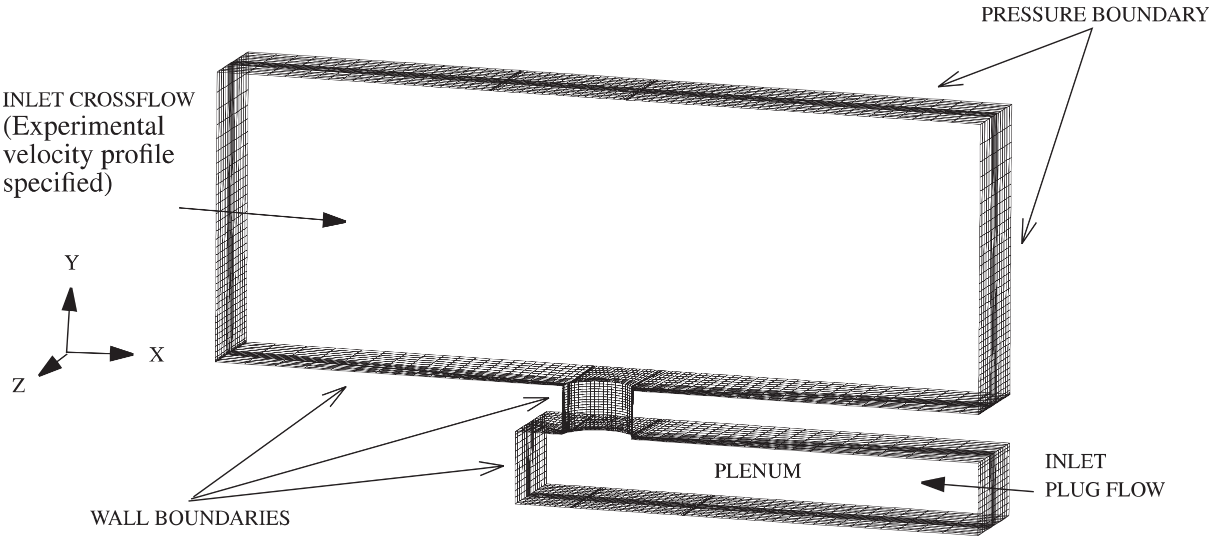

Fig. 3. Computational domain.

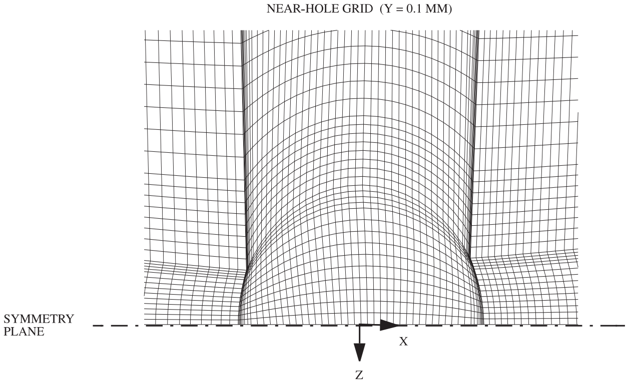

Fig. 4. Top view of near-hole grid distribution (1/2 grid density shown for clarity).

two streams. The k–ε, RNG k–ε, and Reynolds stress turbulence models were examined. Non-equilibrium wall functions and two-layer zonal models were used for near-wall-treatment. These turbulence models and near-wall-treatment methods, as implemented by FLUENT, are discussed in detail by Ferguson et al. (1998) and the theory is presented in an extensive set of user manuals available with the FLUENT software (Fluent, 1997).

Most cases required grids containing approximately 600,000 cells when using wall functions and 900,000 cells when using the two-layer zonal near-wall treatment. Roughly, 60%, 10%, and 30% of the cells are distributed in the crossflow region, the injection hole region and the plenum region, respectively. An overall grid refinement study was performed on the basic geometry by successively doubling the resolution until the solutions varied by less than 0.1% (Hale, 1999). A subsequent grid independence study was performed for each specific configuration by increasing the baseline grid density by 20–30% and tracking changes in the velocity profiles and jet centerline effectiveness. Final grid independence was achieved when predicted centerline effectiveness and jet exit velocity profiles changed by less than 0.1% as the grid density increased by an additional 25%. The grid independence studies were performed for fixed values of y^+ of the wall-adjacent cells. These y^+ values were approximately 1 and 25 for the two-layer zonal model and wall function formulations, respectively.

Different turbulence models and published hydrodynamics and heat transfer data for geometries similar to the current study (e.g., Pietrzyk et al., 1990; Sinha et al., 1991b) were used to evaluate the numerical results. It was concluded that the Reynolds stress model coupled with the two-layer zonal model near wall treatment gave the best results. Typically two weeks of computational time were required on an IBM RS 6000 workstation to obtain a solution for the full Reynolds stress two-layer zonal model with 900,000 cells. All numerical results presented here were obtained using the Reynolds stress-two-layer-zonal model. Detailed comparisons of the turbulence models performance are presented in Hale et al. (1999b).

The assumed symmetry and time-averaging are two limitations of the simulations. Recent work by Smith and Mungal (1998) and Cusano and Plesniak (1999) shows that the jet-in-crossflow structures are unsteady and asymmetric (in the mean) under certain conditions. However, the simulations were adequate to yield insight regarding the role of coherent structures on the measured surface streaklines and heat transfer coefficient data.

Despite their limitations, steady numerical simulations have been used extensively to study the structural features of the jet–crossflow interaction in short hole cases by Garg and Rigby (1998), Berhe and Patankar (1996), and Walters and Leylek (1996). A time-averaged numerical study by Ajersch et al. (1997) showed good agreement between their time-averaged LDV data and their numerical predictions for $M = 0.5$ to 1.5, $P/D = 3.0$, and $L/D = 5.0$.

Our purpose in presenting the results of time-averaged simulations is to relate the time-averaged coherent structures to measured time-averaged quantities (including the surface shear pattern and the heat transfer coefficient). The surface streaks and surface isotherms observed during the experiments were indeed steady. In addition to being steady, the surface streaks and the isotherms were also symmetric in almost all cases. The predicted time-averaged flow structures were in agreement with those observed in the flow visualization studies. Furthermore, structural features observed in other experimental studies for jets in crossflow, and film cooling applications agree with our time-averaged predictions (cf. Haven and Kurosaka, 1997; Gogineni et al., 1996).

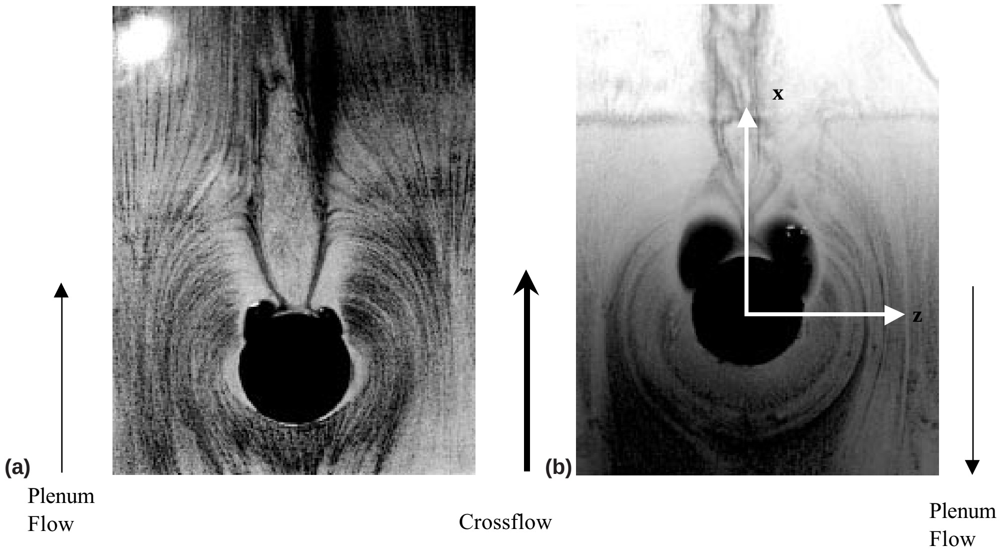

Fig. 5. Surface streaks surrounding interior jet for 90° short cases at $M = 1.0$: (a) co-flow plenum; (b) counter-flow plenum.

6. Results

A large parameter space was explored in the study, but only the results of a few specific configurations will be discussed here due to space limitations. Complete details are available in Hale (1999). Note that the computations, flow visualizations, and heat transfer experiments were all carried out at the same Reynolds numbers.

Figs. 5(a) and (b) show the results of the surface streak experiments for two cases of interest. The cases will be referred to as "90° short co-flow" and "90° short counter-flow", respectively. Note that all cases studied consisted of relatively short injection holes by current industrial standards, but here the term "short" refers to the shortest injection holes studied during the parametric study $(L/D = 0.66)$. These surface streak patterns are related to the mean surface shear stress distributions (dark regions where the tracer accumulates are associated with separation events accompanied by low shear stress). Several interesting features are observable, including: the circular band(s) at the leading edge of the jet hole (lower portion of the photos), the two circular pools of tracer located outboard of the spanwise centerline at the trailing edge of the hole, and the elongated streamwise "streaks" extending downstream of the hole on either side of the centerline, with a clear region in between.

The corresponding topological maps inferred from the surface streak data are presented in Figs. 6(a) and (b). A complete discussion of applications of geometric surface topology to surface streak data is given in Hale (1999). The geometric surface topological rules used to evaluate the possible flow fields are consistent with those reported by Lighthill (1963), Hunt et al. (1978), Tobak and Peake (1979), Chapman (1986), Unal (1987), and Davis (1990). The Euler characteristic, $X(M) = \sum \text{nodes} - \sum \text{saddles} = -1$ for the region visualized in Fig. 5 and analysed in Fig. 6. Caution must be used in evaluating the Euler characteristic of the jet-in-crossflow region, because critical points on the surface map can be inside the injection hole if separation or recirculation exist inside the hole.

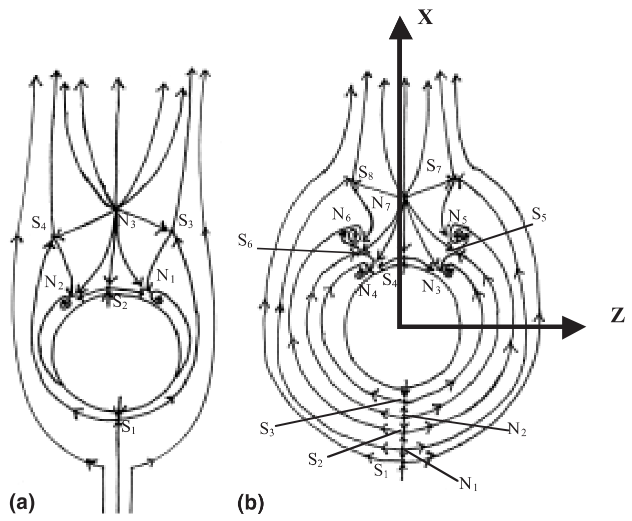

Fig. 6. Topological maps for 90° short cases at $M = 1.0$: (a) co-flow plenum; (b) counter-flow plenum.

It is obvious by comparing the cases in Figs. 5 and 6 that the change in the plenum-flow direction significantly affects the flow field and therefore the resulting surface topological map. The upstream node-saddle pairs in Fig. 6 (corresponding to the upstream circular bands in Fig. 5) are the signatures of the horseshoe vortices captured in the side view (x–y plane) flow visualization and the numerical study shown in Figs. 7(a) and (b), respectively. The approach boundary layer in the counter-flow case is more "distrupted", i.e., the separated flow region extends further upstream of the jet and has greater spanwise extent around the sides of the jet. The series of horseshoe vortices present in the counter-flow case is shown in Fig. 7 (configuration represented in Figs. 5(b) and 6(b)). The image in Fig. 7(a) is a frame from a high-speed video, which was taken at 2000 frames per second. The smoke-seeded boundary layer was illuminated with an argon-ion laser sheet along the centerline plane of the jet. The figure is shown to provide a direct comparison between the experiments and numerical computation, as well as to provide an explanation for the observed topological maps. The number of horseshoe vortices and their location was found to vary with flow conditions, and in some cases there was ingestion of boundary layer fluid into the jet hole. In all cases investigated, the horseshoe vortices were

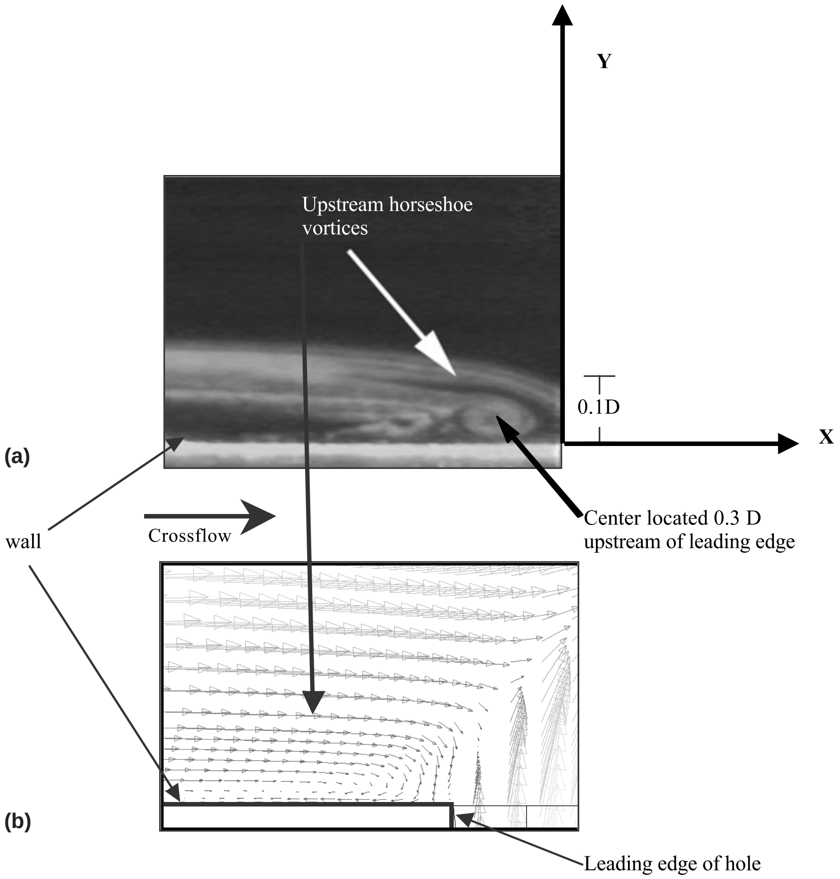

Fig. 7. Upstream horseshoe vortices: (a) experimentally observed; (b) computed ($\alpha = 90^\circ, M = 1.0$, counter-flow plenum).

found to be weak structures that dissipate quickly as their legs wrap around the jet.

The spiral nodes in the downstream region of Fig. 6 (pools of tracer in the trailing edge region of the holes in Fig. 5) correspond to the time-averaged separation related to the wake vortices. The location of the surface signature of the vortices is different in the two cases. There is one pair of time-averaged nodes ($N_{1,2}$) for the co-flow plenum case, and two pairs ($N_{3,4\&5,6}$) of separation nodes in the counter-flow plenum case. Both cases have an attachment region in the wake region of the jet: N_3 for the co-flow case and N_7 in the counter-flow case. It is expected that the convective heat transfer coefficient will be enhanced in regions of attachment and be degraded in regions of separation.

The separation event along the separatrix, i.e., dividing line about which skin friction lines do not cross (line connecting the saddle point to the nodes of separation, saddle points $S_{5,6\&7,8}$ for the counter-flow case and $S_{3,4}$ for the co-flow plenum configuration), is consistent with the separation event reported by Fric and Roshko (1994) in their discussion of wake vortices. The wake vortices originate on the downstream side of the jet due to the roll-up of wall normal vorticity present in the near-jet wake region as the boundary layer fluid sweeps around the issuing jet. The structures are advected downstream, sweeping fluid up from the wall to the underside of the bent over jet; and appear to bend over, align, and combine with the counter-rotating vortex pair (CRVP) downstream.

Our computational results show that the wake vortex and the CRVPs are strongly coupled with the vorticity inside the hole and the vorticity at the jet–crossflow interface near the edge of the hole. A system of vortices forms inside the plenum, with the sense of rotation dependent on the orientation of the plenum, and persists into the injection hole. The vortices may or may not persist through the hole, depending on the flow conditions of the specific case. The predicted velocity fields in the near-wall region agree well with the topology maps inferred from the surface streak experiments, see Hale (1999).

The surface streaks and topology maps for the co-flow plenum case in Figs. 5(a) and 6(a) show an attachment region (region between the two dark streaks downstream of the hole) along the centerline of the jet rather than the expected line of separation associated with the sense of rotation of the primary CRVP. The sense of rotation of the primary CRVP induces a common flow up between the two vortices at the spanwise centerline and down flow outboard of the vortices. Therefore, a separation region is expected between the CRVP and a reattachment region off the centerline, opposite to what is found in Fig. 5(a). The complementary numerical simulations and results from other experiments explain the observed streak pattern. The simulations revealed the presence of a secondary CRVP located below the primary pair and with the opposite sense of rotation for the co-flow configuration. Secondary vortex pairs have been reported previously in the literature, but not nearly as frequently as the main pair, and there has been lack of consensus regarding their origin. For example, Morton and Ibbetson (1996) speculated that two pairs of counter-rotating vortices identified by Andreopoulos and Rodi (1984) to be the CRVP and the legs of the horseshoe vortex for turbulent jet in crossflow. Kelso et al. (1996) also found a second pair of vortices originating outboard of the jet (for low Reynolds number jets) with the same sense of rotation as the legs of the horseshoe vortices (or opposite that of the CRVP).

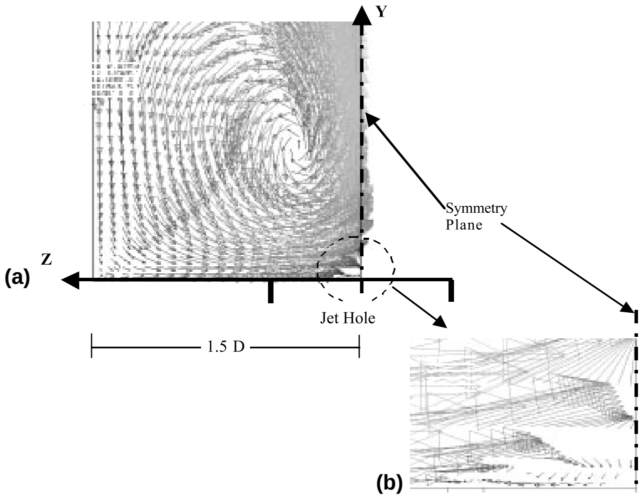

Fig. 8. Main and secondary CRVP $(x/D = 3.0)(\alpha = 90^\circ, M = 1.0,$ co-flow plenum): (a) main CRVP; (b) second CRVP.

Brizzi et al. (1997) identified the second pair as "Werle" vortices in laminar jets in crossflow. Secondary vortex pairs (termed wall wake vortices) were predicted in LES simulations and related to the horseshoe vortices by Yuan (1997), Yuan and Street (1998), and Yuan et al. (1999) for turbulent jets in crossflow. Although these structures are difficult to visualize experimentally, Zheng et al. (1999) recently reported hydrogen bubble flow visualizations and velocity measurements of a similar secondary pair of vortices in a jet in crossflow over a range of velocity ratios of 0.8–3.9 and jet Reynolds numbers of 980–2000. They found that these structures persist from the trailing edge of the jet orifice to at least 7-jet diameters downstream.

Fig. 8(a) shows the cross plane velocity vectors from the numerical computation for the co-flow plenum configuration, with the main flow coming out of the page. Only one half of the pair is shown about the plane of symmetry. The circular motion induced by the primary CRVP is apparent in the velocity vectors and there is a hint of activity in the lower right hand corner. Fig. 8(b) shows a magnified view of this region and reveals the secondary CRVP, with a sense of rotation opposite to that of the primary pair. The wall signature of the secondary pair is the line of attachment observed in the surface streak distributions. A numerical study by Ersoy and Walker (1986), which considered the motion of a pair of counter-rotating vortices above a wall, reported that the pair always induces separation, and in some cases causes the formation of a secondary pair of eddies (when the vortices have a sense of rotation that causes them to move away from the wall).

In the present case, it was found that the trajectory of the CRVP was quite different for the co-flow and counter-flow cases. In the former, the jet is lifted off of the wall and has a well-developed, strong primary CRVP, while in the latter the jet trajectory is shallow so that it does not lift as high off of the wall and has a much weaker CRVP. The trajectories influence not only the separation events but also the formation of the secondary CRVP. Jet trajectories, inferred from seeding the jet with smoke and recording the spreading of the smoke in videos

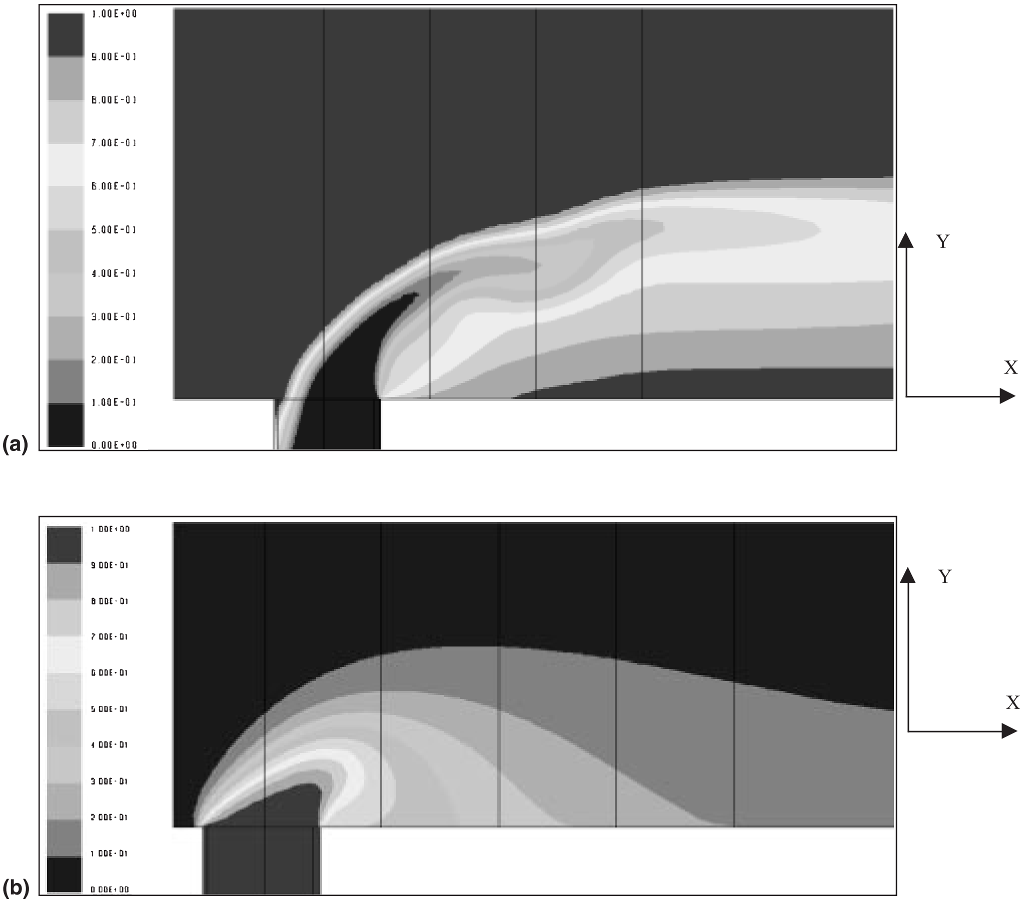

Fig. 9. Numerically-predicted jet trajectories marked by passive scalar concentration for 90° short injection holes, along jet spanwise centerline $(M = 1.0)$: (a) co-flow plenum; (b) counter-flow plenum.

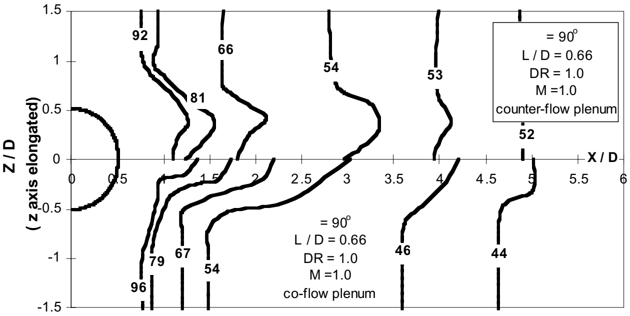

Fig. 10. Convective heat transfer coefficient contours (h[W/m^{2}K]) for short hole 90° cases at $M = 1.0$.

and still photographs, clearly showed the effects of plenum flow direction. The companion numerical studies also illustrated this difference. Fig. 9 shows a comparison of the computed trajectory of the two configurations. Plotted are contours of a passive scalar. In each case, the jet and freestream fluid were assigned values of 0 and 1, intermediate values represent regions where the streams have mixed. This technique qualitatively reveals the jet trajectory by marking its boundary. The results are consistent with the flow visualizations. The relative strength of the attachment events, and therefore the effect on h, is dependent on the trajectory of the primary CRVP, presence or absence of the secondary CRVP, and the attachment of crossflow fluid which has accelerated around the issuing jet.

Fig. 10 shows the contours of constant surface heat transfer coefficient (h). The counter-flow data are presented on the upper half of the plot, while the co-flow data are presented on the lower half of the figure so that side-by-side comparisons may be made. Note that the contours for each case were generally symmetric about the spanwise centerline, so only one-half plane of the measured data is plotted. Any asymmetry (indicated by $\mathrm{d}h/\mathrm{d}z \neq 0$ at $z = 0$) was confined to the neighborhood of the centerline and is believed to be caused by lack of spatial resolution in that region. Figs. 5 and 6 indicated that the attachment region downstream of the hole (cleared out region between the lines of separation) was larger for the co-flow plenum; the case corresponding to a stronger secondary CRVP. Therefore, more centerline heat transfer coefficient enhancement is expected (iso-h lines pushed downstream). This is apparent along the centerline region in Fig. 10. The topological maps also show that the approach boundary layer is more disrupted for the counter-flow case. This is expected to increase the magnitude of the convective heat transfer coefficients in the downstream region and affect a larger spanwise region downstream of the injection holes. These trends are evident when the spanwise extent of the affected region and relative h magnitudes are compared in Fig. 10.

Strong off-center heat transfer coefficient enhancement is observed for the counter-flow case. This is consistent with the improved coverage of the region downstream of the jets observed by Hale (1999). The "enhancement region" is associated with the sweeping of crossflow fluid to the wall. The crossflow fluid must accelerate around the region effectively blocked by the jet fluid and then attaches to the wall in the off-centerline region of enhancement downstream of the jet. The attaching fluid reduces the thickness of the thermal boundary layer and increases the value of the convective heat transfer coefficient. An example of the sweeping of the crossflow fluid into the region of enhancement for a "lifted" jet with the co-flow plenum is illustrated in Fig. 11, which shows the computed streaklines from the numerical simulation, i.e., locus of particles that were tagged in the post-processing software at specific points in the flow field. Note that the crossflow streaklines sweeping around the jet into the region beneath the jet fluid just downstream of the hole exit.

Fig. 12 shows the difference in the separation event in the very near hole region of the jets along the x–y plane on the spanwise centerline for the two cases compared in Fig. 10. The counter-flow case (with more effective blockage) of the crossflow fluid is associated with stronger separation in the region shown. This, in turn, is associated with a lower convective heat transfer coefficient value than the enhanced off-centerline region (refer to Fig. 10). This effect is absent (see Fig. 10) for the co-flow case where the separation in the very near hole region is more limited, as shown in Fig. 12(b).

The relative values of the convective heat transfer coefficients in the off-centerline enhanced region and the center-line region depend on the jet trajectory, the effective jet coverage

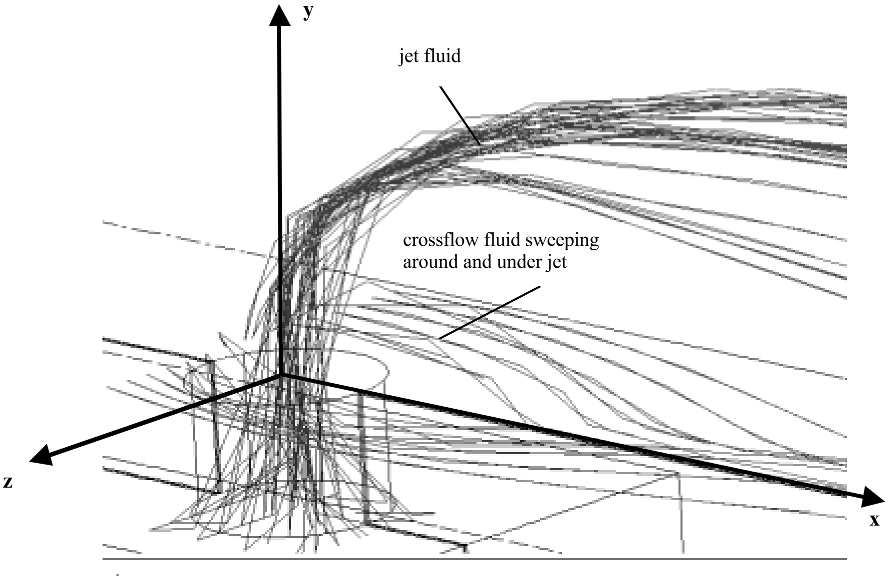

Fig. 11. Streaklines showing attachment regions downstream of injection hole ($\alpha = 90°, M = 1.0$, co-flow plenum).

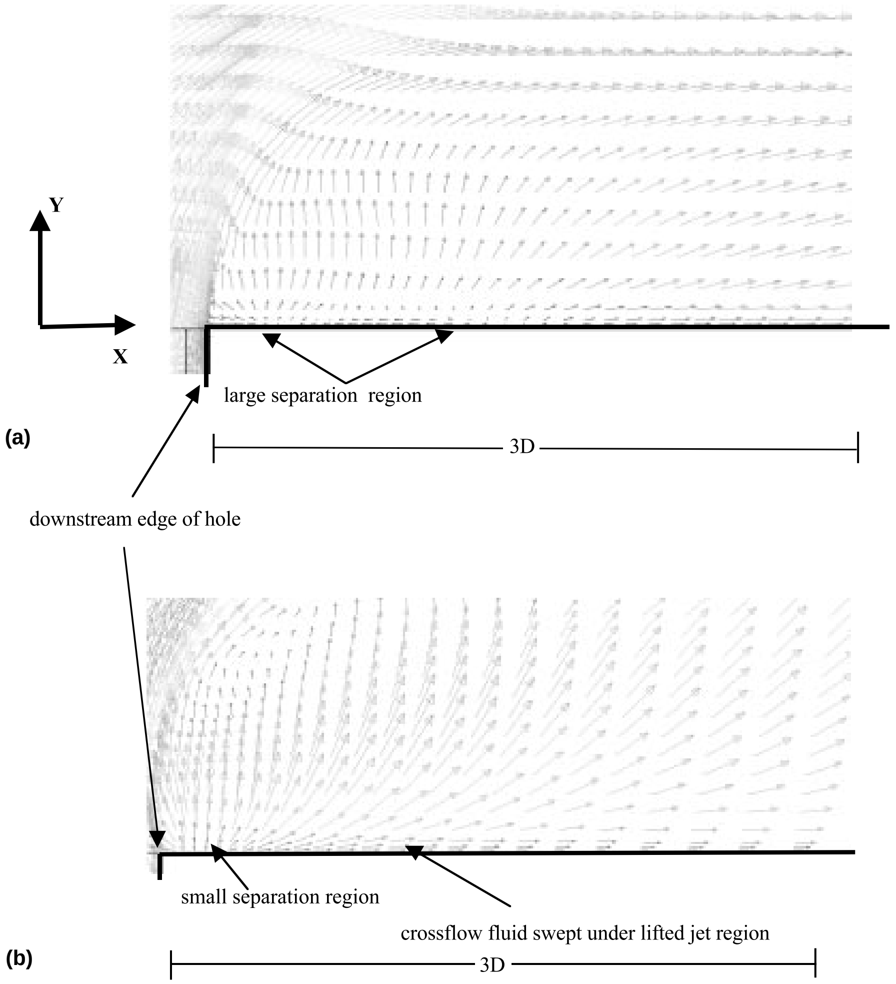

Fig. 12. Separation and attachment regions downstream of 90° short injection holes, along jet spanwise centerline ($M = 1.0$): (a) counter-flow plenum; (b) co-flow plenum.

and resulting blockage of the crossflow, and the strength of the wake vortices. The effect of the plenum flow direction on the surface convective heat transfer coefficient is explained by analysis of the numerically-predicted and experimentally measured changes in the in-plenum, in-hole, and jet–crossflow region flow fields. Detailed discussions concerning the in-plenum and in-hole flow field changes that accompany changes in plenum flow direction are available in Hale (1999).

7. Conclusions

The structures associated with a row of “short-hole” jets injected into a crossflow have been identified experimentally and computed numerically. Upstream boundary layer separation can result in the presence of weak horseshoe vortices, the legs of which are usually dissipated early in the near jet region, for the Reynolds numbers investigated. The upstream boundary layer separation and the attachment zone between separation planes also contributes to the region of streamwise vorticity concentration in the near jet region. The boundary layer fluid roll-up in this region outboard of the jet-boundary layer interface appears to be the origin of the CRVP. The CRVP is intensified in the near jet region by the transfer of momentum from the jet, through viscous interaction or shearing. For some cases, a second pair of counter-rotating vortices develops with the opposite sense of rotation as the CRVP. The secondary pair is located beneath the primary CRVP and is weakly active in sweeping jet fluid toward the wall in the wake region. The existence of a secondary CRVP was inferred from the surface topological maps assembled from the corresponding surface shear stress distributions, as well as numerical predictions. The relative strength of the attachment events, and consequently the effect on h, is dependent on the trajectory of the CRVP, presence or absence of the secondary CRVP, and the attachment of crossflow fluid that has accelerated around the issuing jet. The secondary pair in the co-flow case discussed herein resulted in centerline enhancement of the heat transfer coefficient. The increased disruption of the boundary layer for the counter-flow case resulted in higher spatially-averaged heat transfer coefficient values in the downstream region of the jet.

The use of geometric surface topology revealed the signatures of the horseshoe structures, boundary layer separation, the time-averaged wake vortices, and the secondary CRVP. Combining the topological maps and the surface heat transfer data, enables relatively simple surface streak experiments to qualitatively predict heat transfer enhancement or degradation during parametric studies. The numerical solutions also suggest that the vorticity associated with the wake vortices and the main CRVP are strongly related to the vorticity inside the hole and the vorticity at the jet–crossflow interface near the edge of the hole. The full field data available in the numerical solutions complement the experiments and give more insight into the time-averaged structure of the flow field, which is of interest to the gas turbine industry.

Acknowledgements

We gratefully acknowledge the sustained support of Rolls-Royce/Allison Engine Co. C.A. Hale was supported by Purdue Research Foundation and Ingersoll–Rand fellowships during the course of this research.

References

Ajersch, P., Zhou, J.M., Ketler, S., Salcudean, M., Gartshore, I.S., 1997. Multiple jets in a crossflow: detailed measurements and numerical simulations. Journal of Turbomachinery 119, 330–342.

Andreopoulos, J., Rodi, W., 1984. Experimental investigation of jets in a crossflow. Journal of Fluid Mechanics 138, 93–127.

Berhe, M.K., Patankar, S.V., 1996. A numerical study of discrete-hole film cooling. ASME 96-WA/HT-8.

Bons, J.P., MacArthur, C.D., Rivir, R.B., 1994. The effect of high freestream turbulence on film cooling effectiveness. ASME Paper 94-GT-51.

Brizzi, L., Foucault, E., Bernard, A., Bousgarbles, J., 1997. In the vicinity of a jet in a cross-flow. ASME Paper FEDSM97-3083.

Brundage, A.L., Plesniak, M.W., Ramadhyani, S., 1999. Influence of coolant feed direction and hole length on film cooling jet velocity profiles. ASME Paper 99-GT-035.

Burd, S.W., Simon, T.W., 1997. The influence of film cooling supply geometry on film coolant exit and surface adiabatic effectiveness. ASME Paper 97-GT-25.

Burd, S.W., Simon, T.W., 1998a. Measurements of discharge coefficients in film cooling. ASME Paper 98-GT-009.

Burd, S.W., Simon, T.W., 1998b. Turbulence spectra and length scales measured in film coolant flows emerging from discrete holes. ASME Paper 98-GT-190.

Burd, S.W., Kaszeta, R.W., Simon, T.W., 1996. Measurements in film cooling flows: hole L/D and turbulence intensity effects. ASME Paper 96-WA/HT-7.

Chapman, G.T., 1986. Topological classification of flow separation on three-dimensional bodies. AIAA Paper 86-0485.

Cusano, D.M., Plesniak, M.W., 1999. Asymmetry in a confined rectangular jet in crossflow. In: Proceedings of Turbulence and Shear Flow Phenomena 1999, Paper no. 1–242.

Davis, R.E., 1990. Secondary flow and three-dimensional separation in curved circular ducts. Ph.D. Thesis, School of Aeronautical Engineering, Purdue University.

Ersoy, S., Walker, J.D.A., 1986. Flow induced at a wall by a vortex pair. AIAA Journal 24 (10), 159–1605.

Ferguson, J.D., Walters D.K., Leylek, J.H., 1998. Performance of turbulence models and near-wall treatments in discrete jet film cooling simulations. ASME Paper 98-GT-438.

Findlay, M.J., Salcudean, M., Gartshore, I.S., 1999. Jets in a crossflow: effects of geometry and blowing ratio. ASME Journal of Fluids Engineering 121, 373–378.

Fluent Inc., 1997. FLUENT User's Guide.

Fric, T.F., Roshko, A., 1994. Vortical structure in the wake of a transverse jet. Journal of Fluid Mechanics 279, 1–47.

Garg, V.K., Rigby, D.L., 1998. Heat transfer on a film-cooled blade – effect of hole physics. ASME Paper 98-GT-404.

Gogineni, S.P., Rivir, R.B., Pestian, D.J., Goss, L.P., 1996. PIV measurements of flat plate film cooling flows with high free stream turbulence. AIAA 96–0617.

Gritsch, M., Schulz, A., Wittig, S., 1997. Adiabatic wall effectiveness measurements of film-cooling holes with expanded exits. ASME Paper 97-GT-164.

Hale, C.A., 1999. Short hole film cooling hydrodynamics and convective heat transfer in the near-hole region. Ph.D. Thesis, School of Mechanical Engineering, Purdue University.

Hale, C.A., Plesniak, M.W., Ramadhyani, S., 1999a. Film cooling effectiveness for short holes fed by a narrow plenum. ASME Paper 99-GT-036 (also accepted to appear in ASME Journal of Turbomachinery).

Hale, C.A., Plesniak, M.W., Ramadhyani, S., 1999c. Structural features and surface heat transfer associated with a row of short-hole jets in crossflow. In: Proceedings of Turbulence and Shear Flow Phenomena 1999, Paper No. 1–243.

Hale, C.A., Ramadhyani, S., Plesniak, M.W., 1999b. Film cooling effectiveness predictions for short holes fed by a narrow plenum. ASME Paper 99-GT-162.

Haven, B.A., Kurosaka, M., 1997. Kidney and anti-kidney vortices in crossflow jets. Journal of Fluid Mechanics 352, 27–64.

Hunt, J.C.R., Abell, C.J., Peterka, J.A., Woo, H., 1978. Kinematical studies of the flows around free or surface-mounted obstacles: applying topology to flow visualization. Journal of Fluid Mechanics 86 (1), 179–200.

Kelso, R.M., Lim, T.T., Perry, A.E., 1996. An experimental study of round jets in cross-flow. Journal of Fluid Mechanics 306, 111–144.

Kelso, R.M., Lim, T.T., Perry, A.E., 1998. New experimental observations of vortical motions in transverse jets. Physics of Fluids 10 (9), 2427–2429.

Kohli, A., Bogard, D.G., 1995. Adiabatic effectiveness, thermal fields, and velocity fields for film cooling with large angle injection. ASME Paper 95-GT-219.

Kohli, A., Thole, K.A., 1997. A CFD Investigation on the effects of entrance crossflow direction to film-cooling holes. In: ASME Proceeding of the 32nd National Heat Transfer Conference 12, 223–232.

Kohli, A., Thole, K.A., 1998. Entrance effects on diffused film cooling holes. ASME Paper 98-GT-402.

Lighthill, M.J., 1963. Laminar boundary layers. In: Yousuff Hussaini, M. (Ed.), Collected Papers of Sir James Lighthill, vol. II. Oxford University Press, 1997 (Chapters 1&2).

Margason, R.J., 1993. Fifty years of jet in cross flow research. AGARD-CP-534 November 1993.

Morton, B.R., Ibbetson, A., 1996. Jets deflected in a crossflow. Experimental Thermal and Fluid Science 12, 112–133.

Pietrzyk, J.R., Bogard, D.G., Crawford, M.E., 1989. Hydrodynamic measurements of jets in crossflow for gas turbine film cooling applications. Journal of Turbomachinery 111, 139–145.

Pietrzyk, J.R., Bogard, D.G., Crawford, M.E., 1990. Effects of density ratio on the hydrodynamics of film cooling. Journal of Turbomachinery 112, 437–443.

Schmidt, F.L., Sen, B., Bogard, D.G., 1994. Film cooling with compound angle holes: adiabatic effectiveness. ASME Paper 94-GT-312.

Sen, B., Schmidt, D.L., Bogard, D.G., 1994. Film cooling with compound angle holes: heat transfer. ASME Paper 94-GT-311.

Sinha, A.K., Bogard, D.G., Crawford, M.E., 1991b. Film-cooling effectiveness downstream of a single row of holes with variable density ratio. Journal of Turbomachinery 113, 442–449.

Smith, S.H., Mungal, M.G., 1998. Mixing structure and scaling of the jet in crossflow. Journal of Fluid Mechanics 357, 83–122.

Thole, K.A., Gritsch, M., Schulz, A., Wittig, S., 1996. Flowfield measurements for cooling holes with expanded exits. ASME Paper 96-GT-174.

Thole, K.A., Gritsch, M., Schulz, A., Wittig, S., 1997. Effect of a crossflow at the entrance to a film-cooling hole. Journal of Fluids Engineering 119, 533–540.

Tobak, M., Peake, D.J., 1979. Topology of two-dimensional and three-dimensional separated flows. AIAA Paper 79–1480.

Unal, A., 1987. Three-dimensional singular points in aerodynamics. NASA TM-100045, USAAVSCOM TR-87-A-14.

Walters, D.K., Leylek, J.H., 1996. A systematic computational methodology applied to a three-dimensional film-cooling flowfield. ASME Paper 96-GT-351.

Walters, D.K., Leylek, J.H., 1997. A detailed analysis of film-cooling physics. Part I: Streamwise injection with cylindrical holes. ASME Paper 97-GT-269.

Wittig, S., Schulz, A., Gritsch, M., Thole, K.A., 1996. Transonic film-cooling investigations: effects of hole shapes and orientations. ASME Paper 96-GT-222.

Wolochuk, M.C., Plesniak, M.W., Braun, J.E., 1996. The effects of turbulence and unsteadiness on vortex shedding from sharp-edged bluff bodies. ASME Journal of Fluids Engineering 118, 18–25.

Wolochuk, M.C., Plesniak, M.W., Braun, J.E., 1994. Evaluation of vortex shedding flow meters for HVAC applications. Purdue University Report ME-TSPC/HERL-TR-94-1.

Yuan, L.L., Street, R.L., Ferziger, J.H., 1999. Large-eddy simulations of a round jet in crossflow. Journal of Fluid Mechanics 379, 71–104.

Yuan, L.L., Street, R.L., 1998. Trajectory and entrainment of a round jet in crossflow. Physics of Fluids 10 (9), 2323–2335.

Yuan, L.L., 1997. Large eddy simulations of a jet in crossflow. Ph.D. Thesis, Department of Mechanical Engineering, Stanford University.

Zheng, Q., Klewicki, J., McMurtry, P., 1999. Near wall counter-rotating vortex pair in the wake region of a transverse jet in crossflow. Bulletin of the American Physical Society, Division of Fluid Dynamics 44 (8), 110.